## Advances in Geo-Energy Research

#### Original article

# Influence of thermodynamic and stress conditions in saline aquifers on CO<sub>2</sub> drainage: Optimization of CO<sub>2</sub> storage and energy recovery

Mengqiu Yan<sup>1,2</sup>, Zhao Lu<sup>2,30</sup>\*, Xin Yang<sup>4,5</sup>, Jia-nan Zheng<sup>6</sup>, Lizhong Wang<sup>1,2</sup>, Yi Hong<sup>20</sup>\*

#### **Keywords:**

CO<sub>2</sub> geological storage residual water saturation CO<sub>2</sub> phase displacement efficiency capillary pressure

#### Cited as:

Yan, M., Lu, Z., Yang, X., Zheng, J., Wang, L., Hong, Y. Influence of thermodynamic and stress conditions in saline aquifers on CO<sub>2</sub> drainage: Optimization of CO<sub>2</sub> storage and energy recovery. Advances in Geo-Energy Research, 2025, 18(3): 207-217. https://doi.org/10.46690/ager.2025.12.01

#### Abstract:

The accumulation of immobile residual water during CO<sub>2</sub> injection for brine displacement significantly impairs storage efficiency, injectivity, and fluid migration—key factors for scaling up CO<sub>2</sub>-based energy technologies. This study investigates the factors governing residual water saturation under different CO2 phases and effective stress conditions in simulated subsurface environments. The results indicate that under constant effective stress, gaseous CO<sub>2</sub> vields the highest residual water saturation, followed by its supercritical and liquid states. As such, an inverse relationship is observed between residual water saturation and storage efficiency/capacity, underscoring the potential for jointly optimizing energy recovery and CO<sub>2</sub> sequestration. The analysis of the CO<sub>2</sub>-brine-rock system confirms that capillary forces control residual water saturation. Increased interfacial tension or contact angle cosine value raises capillary entry pressure, hindering displacement and elevating irreducible water saturation. Moreover, higher effective confining pressure reduces capillary radius and creates "dead pores", thereby increasing capillary pressure and enhancing water trapping in the core. The findings give critical insights into how CO2 phase behavior and confining pressure govern residual water saturation, displacement efficiency and migration in the reservoir, directly informing strategies for optimal CO<sub>2</sub> storage reservoir selection and enhanced oil recovery operations.

#### 1. Introduction

CO<sub>2</sub> geological storage plays a pivotal role in supporting energy transition and achieving carbon reduction goals, offering great potential for enhancing energy security and enabling CO<sub>2</sub> utilization in subsurface systems (Aminu et al., 2017; Cai and Berg, 2025). Suitable storage sites include unminable coal seams (Mazzotti et al., 2010), depleted oil

and gas reservoirs (Samara et al., 2019), saline aquifers (Sun et al., 2021), and marine sediments (Leung et al., 2014). Among them, saline aquifers are considered a prime candidate for CO<sub>2</sub> geological sequestration because of their widespread occurrence and significant volumetric potential (Vilarrasa et al., 2013; Kim et al., 2021). The sequestration process involves multiple mechanisms, with CO<sub>2</sub> displacing brine in

Yandy Scientific Press  $\ ^{*}Corresponding \ author.$ 

E-mail address: ymq6463@163.com (M. Yan); zhaolu@ust.hk (Z. Lu); yangxin\_zju@foxmail.com (X. Yang); zhengjn@zju.edu.cn (J. Zheng); wanglz@zju.edu.cn (L. Wang); yi\_hong@zju.edu.cn (Y. Hong). 2207-9963 © The Author(s) 2025.

Received September 10, 2025; revised October 6, 2025; accepted October 21, 2025; available online October 25, 2025.

<sup>&</sup>lt;sup>1</sup>Ocean College, Zhejiang University, Zhoushan 316021, P. R. China

<sup>&</sup>lt;sup>2</sup>Hainan Institute of Zhejiang University, Sanya 572025, P. R. China

<sup>&</sup>lt;sup>3</sup>HKUST Shenzhen-Hong Kong Collaborative Innovation Research Institute, Shenzhen 518000, P. R. China

<sup>&</sup>lt;sup>4</sup>College of Civil Engineering and Architecture, Zhejiang University, Hangzhou 310058, P. R. China

<sup>&</sup>lt;sup>5</sup>Institute for Smart City of Chongqing University in Liyang, Chongqing University, Jiangsu 213300, P. R. China

<sup>&</sup>lt;sup>6</sup>Shanghai Institute for Advanced Study, Zhejiang University, Shanghai 201203, P. R. China

reservoir pores (drainage) and subsequent capillary trapping and imbibition (Lu et al., 2025a). In particular, the drainage process serves as the crucial initial phase for efficient CO<sub>2</sub> storage and energy-related applications (Xu et al., 2020; Lu et al., 2025b). However, during CO<sub>2</sub> injection for brine displacement, capillary forces and hydrophilic mineral interactions result in a significant fraction of residual water becoming trapped within the pores (Li et al., 2017). This immobile water can account for 30% to 50% of pore space, substantially reducing the effective CO<sub>2</sub> storage capacity and thus limiting the efficiency of CO<sub>2</sub> utilization for enhanced energy production (Al-Zaidi et al., 2019). Moreover, the accumulation of residual water can elevate reservoir pressure and dissolve cap rock minerals, thereby increasing the risks of geological hazards and compromising the sealing integrity of the cap rock (Jayasekara et al., 2020). These processes pose risks to longterm CO<sub>2</sub> storage security, hence it is critical to understand the mechanisms and influencing factors of residual water formation to ensure safe and effective carbon sequestration (Zhang et al., 2022).

The presence of residual water in saline aquifers is governed by the combination of rock properties, fluid characteristics, and the formation environment (e.g., temperature, pressure, and brine chemistry) (Bachu and Bennion, 2009; Bachu, 2015). The key characteristics in the CO<sub>2</sub>-water-rock system, including interfacial tension, wettability, and viscosity ratio, affect the entire displacement process. Interfacial tension is an important factor governing two-phase flow displacement (Saraji et al., 2014), which varies significantly with pressure, temperature and brine salinity. As the interfacial tension increases, the capillary entry pressure required for CO<sub>2</sub> drainage also increases, thereby elevating the residual water saturation (Li et al., 2017). Wettability is dictated by the properties of both the rock and the fluid (Singh et al., 2016; Pan et al., 2019). However, the impact of contact angle on residual water formation remains unclear. Furthermore, changes in temperature and pressure modify the viscosity ratio and density difference, which subsequently affect interfacial tension, wettability, capillary number, and relative permeability (Basirat et al., 2017; Zadeh et al., 2024). Specifically, high viscosity and capillary number lead to stable displacement; low viscosity causes viscous fingering; and a low capillary number results in capillary fingering, with the relative permeability of CO<sub>2</sub> generally decreasing as the capillary number rises (Amiri and Hamouda, 2014; Zeng et al., 2025). Overall, the synergy of these characteristics determines the formation mechanism of residual water.

In practical CO<sub>2</sub> geological storage, formation depth governs the *in-situ* temperature and pressure, which subsequently determine the CO<sub>2</sub> phase behavior and the effective confining pressure (Al-Zaidi et al., 2018). These coupled thermodynamic and geomechanical conditions directly impact CO<sub>2</sub> displacement efficiency, migration velocity, and long-term storage integrity (Amiri and Hamouda, 2014). While drainage processes involving supercritical CO<sub>2</sub> have been investigated extensively, the current understanding remains predominantly based on studies conducted under a single, constant effective confining pressure. Pioneering work using

advanced techniques such as NMR (Xu et al., 2020) and X-ray imaging (Kim et al., 2018; Shi et al., 2011) has significantly advanced the knowledge of supercritical CO2 displacement, revealing underlying mechanisms such as viscosity differenceinduced fingering and preferential invasion through larger pores due to capillary pressure effects. These studies, along with pore-scale analyses, have consistently demonstrated that the displacement process is primarily dominated by capillary fingering mechanisms at low capillary numbers (Herring et al., 2014; Ragui and Chen, 2023; Cai et al., 2025), with CO<sub>2</sub> plume morphology and cluster distribution being further influenced by viscosity ratios and capillary numbers (Kuo and Benson, 2015; Yang et al., 2023). A closer examination of the existing literature, however, indicates that the combined effects of CO<sub>2</sub> phase state, which spans gaseous, supercritical, and liquid forms depending on the reservoir conditions (Al-Zaidi et al., 2018), and the dynamic changes in effective confining pressure induced by injection, have not received sufficient attention. The comparative impacts of different phases on residual water saturation remain poorly understood, and the systematic influence of stress variations on drainage efficiency is yet to be thoroughly explored. Therefore, a comprehensive understanding of how these two interdependent variables, i.e., CO<sub>2</sub> phase and effective stress, govern residual water formation is crucial for predicting and optimizing sequestration performance.

In view of the aforementioned research gap, this study systematically investigates the phase-stress interdependence through high-pressure/high-temperature core-flooding experiments. The objective is to quantify the coupled effects of CO<sub>2</sub> phase (gaseous, supercritical, liquid) and effective confining pressures on residual water saturation. The analysis reveals the underlying mechanisms governing water trapping and enables the identification of optimal conditions for storage. The findings provide a quantitative basis for optimizing storage reservoir selection and controlling CO<sub>2</sub> plume migration, thereby enhancing the safety and efficiency of geological carbon sequestration.

#### 2. Experiment

#### 2.1 Core sample and fluid characterization

The experimental materials included deionized water, CO<sub>2</sub> and natural argillaceous sandstone. The sandstone core sample with standard dimensions (50 mm diameter  $\times$  100 mm height) was collected from Cretaceous strata in the Sichuan Basin. The core appeared generally homogeneous and mechanically intact, showing no visible microcracks. Mineralogical analysis via X-ray diffraction identified quartz as the dominant mineral at 40.9%, followed by muscovite at 13.9%, calcite at 16.9%, albite at 11.1%, chlorite at 10.1%, and kaolinite at 7.1% (Fig. 1(a)). The permeability and porosity of the argillaceous sandstone core were measured at 1.51 mD and 9.64%, respectively. Mercury injection capillary pressure (MICP) data (Fig. 1(b)) indicated a peak pore throat diameter of 226 nm with a corresponding frequency of 9.6%. The CO<sub>2</sub> (99.999% purity) was supplied by Huate Gas Co., Ltd. (Foshan, China), and deionized water was provided by Nandai Industrial Co., Ltd.

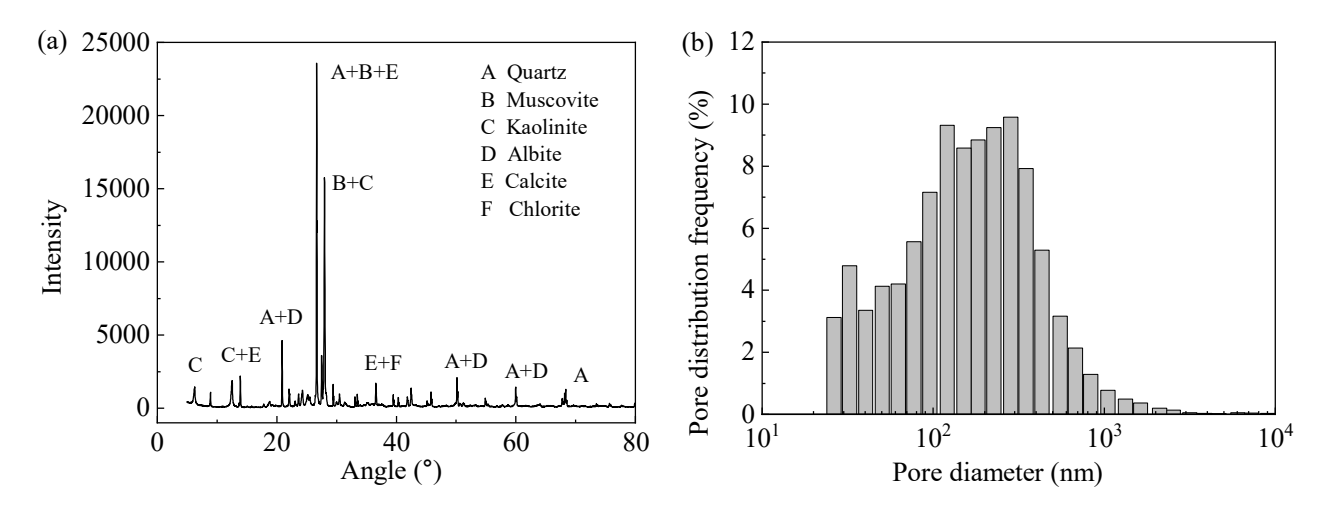


**Fig. 1**. Basic physical parameters of the core sample: (a) Diagram of X-ray diffraction analysis and (b) pore throat distribution of rock sample.

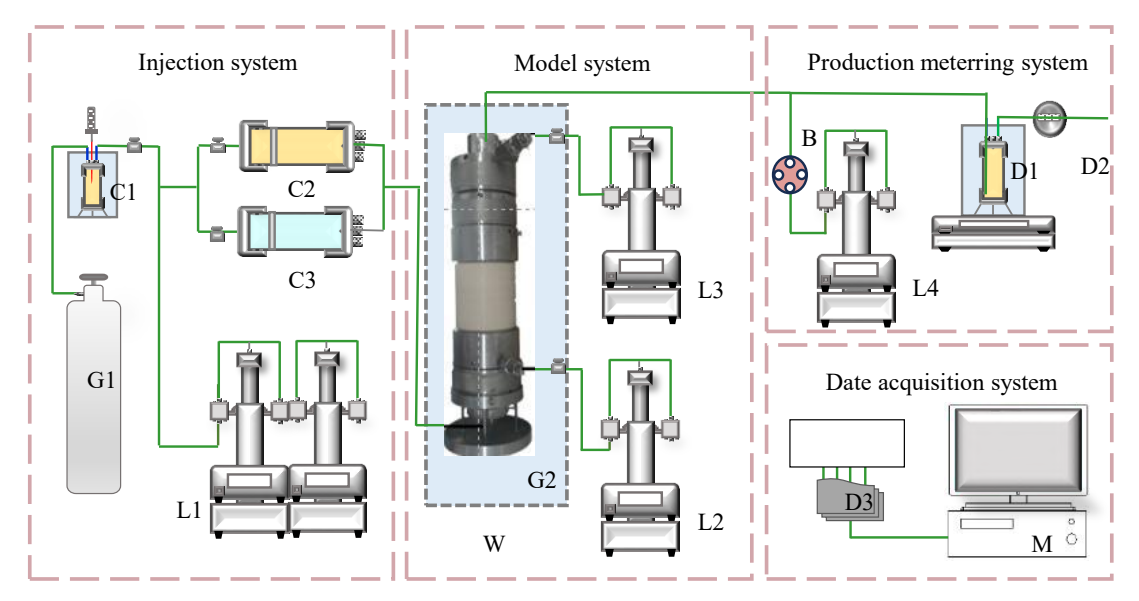


**Fig. 2**. Schematic diagram of the experimental system: C1-Gas storage tank, C2/C3-CO<sub>2</sub>/H<sub>2</sub>O high pressure vessel, L1-Double-cylinder injection pump, G2-Core holder, L2-Loading pump, L3-Confining pump, W-Constant temperature bath, B-Back pressure valve, L4-Back pump, D1-Gas-liquid separator, D2-Gas flowmeter, D3-Data collector, M-Computer.

(Zhejiang, China).

## 2.2 High-pressure/high-temperature experimental apparatus

An experimental apparatus was constructed to reproduce the high-pressure and high-temperature (HPHT) conditions representative of CO<sub>2</sub> geological storage environments. A diagram of this system is presented in Fig. 2. The setup comprises four main subsystems: A model system, an injection system, a production metering system, and a data acquisition system.

A continuous injection pump supplies fluid pressure ranging from 0 to 50 MPa, supporting pulse-free operation in either constant-rate or constant-pressure mode. Confining (axial) pressure is independently regulated by a dedicated pump, with

an operable range of 0-35 MPa and the accuracy is 0.1% of full scale. The core holder and  $CO_2$  vessel are maintained at target temperatures using a water bath, adjustable from 0 to 80 °C with a precision of  $\pm 0.1$  °C.

Produced fluids are processed through a gas-liquid separator, with gas volume measured by a gas flow meter and liquid mass determined by an electronic balance in combination with a silica gel drying tube. The data acquisition system records real-time parameters such as pressure and gas/liquid flow rates, and enables the remote control of pump operation and experimental settings.

#### 2.3 Experimental procedures

In practical carbon sequestration projects, depending on the variations in reservoir pressure and temperature, CO<sub>2</sub> can be

Table 1. Experim	ental conditions of	of CO <sub>2</sub> drainage in	n					
different phases.								
			_					

P (MPa)	T (°C)	CO <sub>2</sub> Phase state	Back pressure (MPa)	Confining pressure (MPa)	Effective confining pressure (MPa)
4	20	Gaseous	4	8	4
				12	8
				16	12
8	40	Supercritical	8	12	4
				16	8
				20	12
8	20	Liquid	8	12	4
				16	8
				20	12

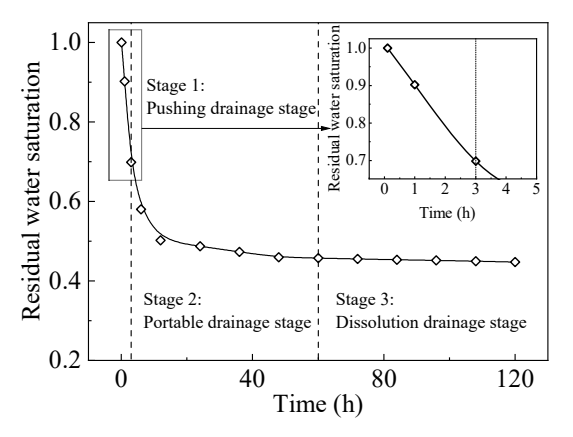


Fig. 3. Schematic diagram of the CO<sub>2</sub> drainage displacement process.

injected in its gaseous, supercritical and liquid forms (Al-Zaidi et al., 2018). The injection process also changes formation stress due to changes in pore pressure. Therefore, displacement experiments were carried out across various CO<sub>2</sub> phase states and effective confining pressures to measure the breakthrough time and the residual water saturation, which is defined as the value when no further reduction was observed. The calculation of residual water saturation is:

$$S_w = \frac{m_2 - m_1}{m_1 - m_0} \times 100\% \tag{1}$$

where  $S_w$  denotes the residual water saturation;  $m_0$  and  $m_1$  represent the dry weight and saturated weight of rock core, respectively;  $m_2$  is the residual weight of rock core after  $CO_2$  displacement of water.

The specific procedures are as follows:

- 1) Dry the core at 105 °C for 12 h to obtain its dry mass  $(m_0)$ . Then, place it under vacuum for over 5 h, pressurize it to 10 MPa with deionized water, and saturate it for 24 h before weighing to determine its saturated mass  $(m_1)$ .
- 2) Install the saturated core into the core holder and set the

- required temperature. Inject CO<sub>2</sub> into the gas tank to the target pressure and stabilize it for 2 h to achieve the desired CO<sub>2</sub> phase. Set the backpressure to the target value and gradually increase the confining pressure according to Table 1, maintaining the difference between them as the effective confining pressure. Use this configuration to regulate the outlet pressure via the backpressure.
- 3) Inject CO<sub>2</sub> of the desired phase into the core using a continuous injection pump, maintaining a pressure difference of approximately 1 MPa across the core. Then, gradually bleed the backpressure down to atmospheric level. Finally, extract the core and determine its mass (*m*<sub>2</sub>), then the residual water saturation can be obtained by Eq. (1).
- 4) Repeat the above procedure under identical conditions, retrieving the core to measure  $S_w$  at 3 and 6 h.
- 5) Continue the displacement for up to 120 h without retrieving the core. Determine the total mass of displaced water by summing the water collected in the separator and the mass increase of the silica gel, recording these measurements at 9, 12, 24, 36, 48, 60, and 120 h. Conclude the experiment by gradually releasing the backpressure to atmospheric level.

#### 3. Results and discussion

### 3.1 Evolution of residual water saturation during drainage

On the basis of the experimental data for residual water saturation over drainage time, one representative curve was selected to illustrate the typical trend, as shown schematically in Fig. 3. The drainage process comprises three distinct stages. The first stage (termed the "pushing drainage stage") lasts for 2-3 hours, during which most pore water is initially displaced. In this stage, capillary forces trap small amounts of water as liquid bridges between particles, while the hydrophilic nature of minerals retains additional water on particle surfaces, preventing complete drying. The second stage (the "portable drainage stage", 0-60 hours in this experiment) involves pore water being either dissolved in or entrained by the CO<sub>2</sub> stream. Finally, the third "dissolution stage" addresses the very small amount of capillary water trapped in pore corners by strong capillary forces (Spycher et al., 2003), which can only be removed through long-term dissolution into CO<sub>2</sub>.

The variations in residual water saturation versus drainage time under different phase states and effective confining pressures are depicted in Fig. 4. Initially, the water saturation in the core drops rapidly from 1.0, and the slope of the curves is steep. Subsequently, the drainage process decelerates as CO<sub>2</sub> invasion occupies the pore space at a diminishing rate, which reduces the efficiency of water expulsion. This results in a gradual decrease in the slope of the curve until the residual water saturation eventually stabilizes and remains constant until the end of the displacement. The temporal decay of residual water saturation under all tested conditions is well-characterized by an exponential decay function (Eq. (2)), which is commonly used to describe such drainage processes:

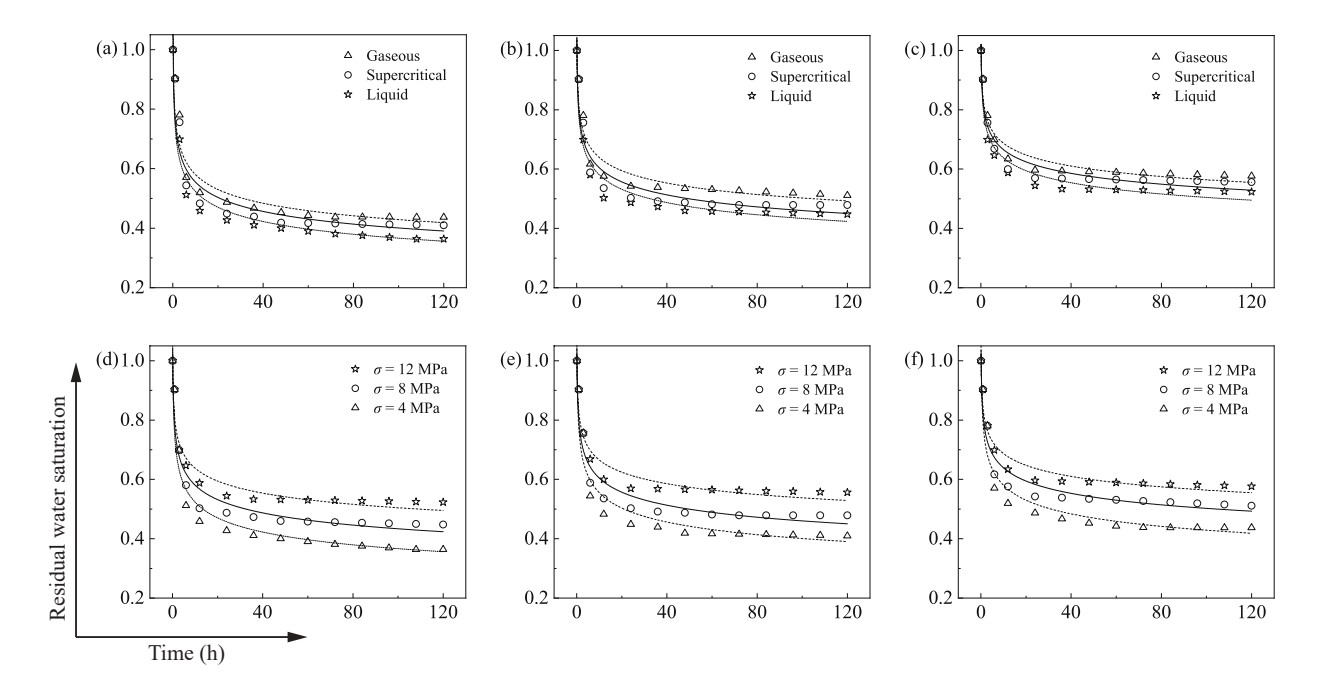


**Fig. 4**. Residual water saturation change curves under different CO<sub>2</sub> thermodynamic states and effective confining pressures: (a) 4 MPa, (b) 8 MPa, (c) 12 MPa, (d) liquid, (e) supercritical, and (f) Gaseous.

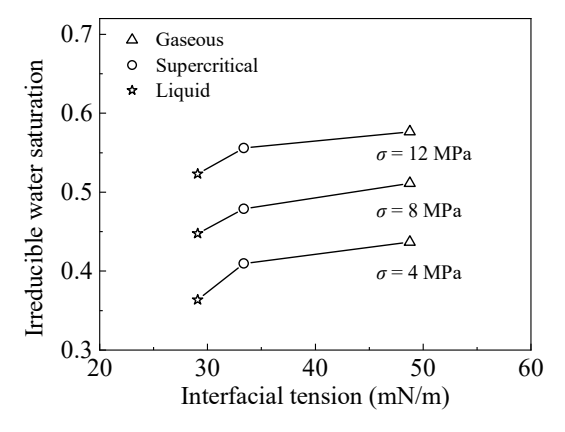


**Fig. 5**. Effects of variation in interfacial tension (Bachu and Bennion, 2009) on irreducible water saturation under different thermodynamic states of CO<sub>2</sub>.

$$S_w = \alpha t^{-\beta} \tag{2}$$

where  $\alpha$  and  $\beta$  are the fitting coefficients; and t denotes the displacement time. During the pushing drainage and portable drainage stages at an effective confining pressure of 4 MPa (Fig. 4(a)), clear differences in residual water saturation are observed after drainage with different  $CO_2$  phases. Specifically, the phase transition of  $CO_2$  from gaseous/supercritical to liquid results in a marked decrease in residual water saturation. In contrast, during the dissolution stage, the variation in residual water saturation with different  $CO_2$  phases is relatively small. Moreover, a similar trend is replicated at effective confining pressures of 8 and 12 MPa (Figs. 4(b) and 4(c)). Furthermore, when liquid  $CO_2$  is used for drainage in the pushing drainage and portable drainage stages (Fig. 4(d)), the difference in residual water saturation under varying effective confining pressures becomes more pronounced. The highest residual

water saturation occurs at 12 MPa, and it decreases as the confining pressure is reduced. Again, the dissolution stage shows minimal variation, and a comparable pattern is observed with supercritical and gaseous  $CO_2$  drainage (Figs. 4(e) and 4(f)). However, as indicated by the spacing between the curves, the influence of effective confining pressure is more significant than that of the  $CO_2$  phase.

#### 3.2 Influence of CO<sub>2</sub> phase state

#### 3.2.1 Interfacial tension analysis

Interfacial tension is the action of two-phase interfaces, which has a crucial implication for the residual water saturation, significantly affecting the storage of  $CO_2$  (Bachu and Bennion, 2009). The correlation of interfacial tension and residual water saturation with three  $CO_2$  phases is shown in Fig. 5. Interfacial tension varies significantly with the phase state, exhibiting the trend of gaseous > supercritical > liquid. Correspondingly, the reduction in interfacial tension directly lowers the residual water saturation. This is because liquid  $CO_2$  and water are mutually highly soluble, which promotes the mixing of the two phases and diminishes the effective intermolecular forces at their interface. The dissolution of  $CO_2$  into the aqueous phase further contributes to this reduction in interfacial tension.

The fluid migration characteristics in porous media are affected by interfacial tension due to its ability to change capillary entry pressure. Capillary storage efficiency, CO<sub>2</sub> migration, and the resulting residual trapping are all governed by the capillary entry pressure, which is expressed by the Laplace equation:

$$P_c = \frac{2\gamma\cos\theta}{R} \tag{3}$$

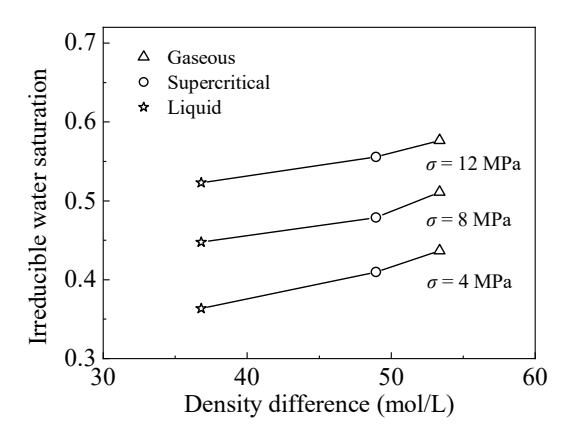


Fig. 6. Effects of variation in density difference on irreducible water saturation under different thermodynamic states of CO<sub>2</sub>.

where  $P_c$  denotes the CO<sub>2</sub> capillary entry pressure; R is the effective pore throat radius;  $\gamma$  is the interfacial tension between water and  $CO_2$ ;  $\theta$  is the water- $CO_2$ -rock contact angle.

On the basis of Laplace's equation, effective pore radius, interfacial tension, and contact angle are the dominant parameters that influence capillary pressure in the porous medium. For a given rock geometry (constant R and  $\theta$ ), capillary pressure increases with interfacial tension. The properties of deionized water and liquid CO<sub>2</sub> are highly matched, enhancing their mutual solubility. The subsequent dissolution of CO<sub>2</sub> into water weakens the intermolecular interactions, reducing interfacial tension. This lowers the capillary entry pressure, facilitating CO<sub>2</sub> migration through the pores and ultimately explaining the remarkably low residual water saturation after liquid CO<sub>2</sub> flooding. Conversely, gaseous and supercritical CO<sub>2</sub> exhibit lower solubility in water (Nomeli and Riaz, 2017), which results in higher residual water saturation after flooding.

#### 3.2.2 Wettability analysis

In the CO<sub>2</sub>-H<sub>2</sub>O-rock system, wettability plays an important role in assessing fluid distribution and transport within the core's pore structure, as well as its capillary storage (Basirat et al., 2017). Wettability is generally explained by contact angle  $\theta$ . However, its experimental determination under HPHT conditions is challenging, often leading to poor accuracy and significant uncertainties. Experimental observations of the contact angle under elevated temperature and pressure have shown varying trends, reporting a consistent increase (Singh et al., 2016), a rising trend between 7-10 MPa followed by stabilization (Jung and Wan, 2012); and in some cases, no significant influence of pressure changes (Saraji et al., 2014). Therefore, to account for the significant discrepancies in experimental CO<sub>2</sub>-water-rock contact angle data, particularly regarding variations in contact angle and density induced by pressure-temperature conditions, the following formula was proposed (Pan et al., 2019):

$$\cos\theta = \frac{I}{\gamma}\Delta\rho - 1\tag{4}$$

where  $\cos \theta$  represents the cosine of the contact angle; I denotes the van der Waals potential energy integral;  $\Delta \rho$ represents the CO<sub>2</sub>-water density difference.  $I/\gamma_{fl}$  remains unchanged with the change in density difference  $\Delta \rho$ .

CO<sub>2</sub> density changes markedly with the thermodynamic conditions, while H<sub>2</sub>O density shows comparatively less variation, resulting in a density difference (Fig. 6) that is greatest under gaseous conditions and becomes progressively smaller for supercritical and liquid  $CO_2$ . The value of  $\cos \theta$  varies linearly with the density difference, where  $I/\gamma_{fl} > 0$ , that is, with the decrease in density difference  $\Delta \rho$ , the  $\cos \theta$  decreases. Therefore, the calculated contact angle cosine is highest in the gaseous, intermediate in the supercritical, and lowest in the liquid. According to Laplace's equation, under otherwise identical conditions, a larger  $\cos \theta$  indicates a higher capillary entry pressure. Consequently, the gaseous phase exhibits the highest capillary entry pressure, the supercritical phase has an intermediate value, and it is the lowest for the liquid phase. This increased entry pressure impedes CO<sub>2</sub> migration through pore throats, leading to greater residual water saturation in the core, a result consistent with displacement experiments under the three phase conditions.

Furthermore, changes in the CO<sub>2</sub> phase behavior also alter the  $\theta$  within the CO<sub>2</sub>-water-rock system, thereby affecting irreducible water saturation. However, the correlation between contact angle and residual water saturation remains contextdependent. For instance, no clear correlation was observed in heterogeneous microfluidic models (Basirat et al., 2017), while an increase in residual water saturation with contact angle has been reported through numerical simulations in uniform porous media (Amiri and Hamouda, 2014). This apparent contradiction suggests that the role of contact angle is likely influenced by pore geometry.

#### 3.2.3 Viscosity ratio analysis

Another key parameter that determines the efficiency of CO<sub>2</sub> storage is the viscosity ratio. The viscosity of CO<sub>2</sub> changes markedly with its phase state, and water viscosity, while being relatively stable, also varies with pressure and temperature (Basirat et al., 2017; Zadeh et al., 2024). Because the viscosity of water is much greater than that of  $CO_2$ , the value of M is very small. This leads to viscous fingering during displacement, which destabilizes the flow front (Kuo and Benson, 2015). The viscosity ratio (M) can be calculated as follows:

$$M = \frac{\mu_i}{\mu_d} \tag{5}$$

 $M = \frac{\mu_i}{\mu_d} \eqno(5)$  where  $\mu_i$  and  $\mu_d$  represent the viscosities of CO<sub>2</sub> and water, respectively.

A further analysis was conducted on the impact of viscosity ratio on residual water saturation, as illustrated in Fig. 7. The viscosity ratio M of  $CO_2$  follows the order of gaseous < supercritical < liquid. As viscosity ratio decreases, residual water saturation increases. During displacement, the higher viscosity of the water compared to the CO2 causes displacement front instability, resulting in viscous fingering. It has been shown that a lower viscosity ratio results in more extensive fingering within the pore network, as demonstrated using the Lattice Boltzmann method (Mejia et al., 2021). This pronounced fingering, along with increased water retention along pore wa-

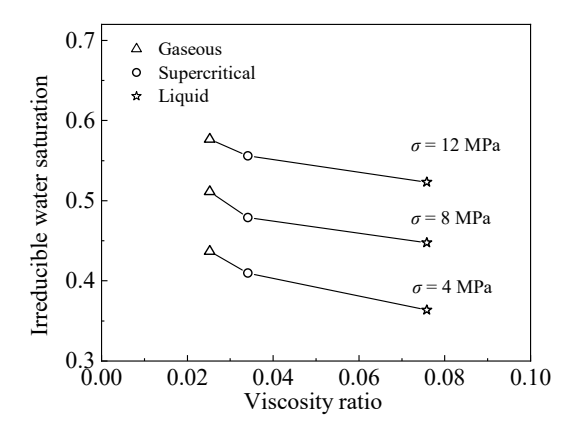
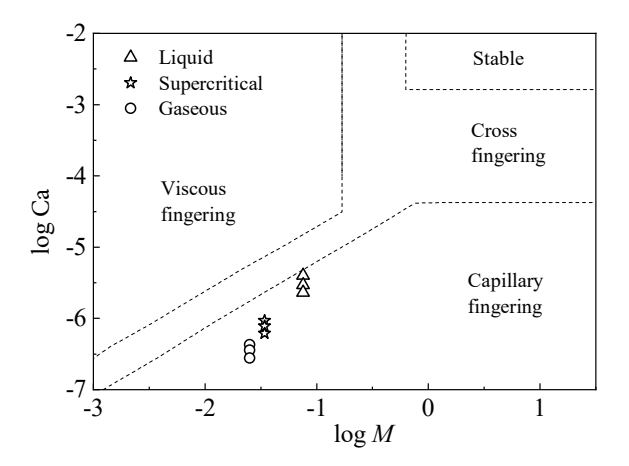


Fig. 7. Effects of variation in viscosity ratio on irreducible water saturation under different thermodynamic states of CO<sub>2</sub>.



**Fig. 8.**  $\log \text{Ca} - \log M$  stability phase diagram (the template and region division are based on the study by Amiri and Hamouda (2014).

lls, reduces displacement efficiency. Thus, the decrease in viscosity ratio promotes residual water saturation by altering the invasion pattern in the pore space.

#### 3.2.4 Phase diagram

The above analysis demonstrates that the thermodynamic state of CO<sub>2</sub> governs residual water saturation by altering the viscosity ratio, interfacial tension, and wettability. Specifically, the progression from gaseous to supercritical to liquid CO<sub>2</sub> is marked by the reduction in both interfacial tension and  $\cos \theta$ . This in turn reduces the capillary entry pressure, leading to a decline in residual water saturation. The concurrent increase in viscosity ratio stabilizes the displacement front by mitigating fingering, which synergistically improves displacement efficiency and further limits water retention. Thus, residual water saturation is collectively determined by these three interacting factors. As a key dimensionless parameter, the capillary number assesses the relative strength of capillary forces to viscous forces (Yiotis et al., 2007; Zeng et al., 2025). To further investigate the influences of capillary forces and viscous forces on the displacement process and thus identify the primary factors affecting the results, a phase diagram was constructed based on the CO<sub>2</sub> displacement experiments (Fig.

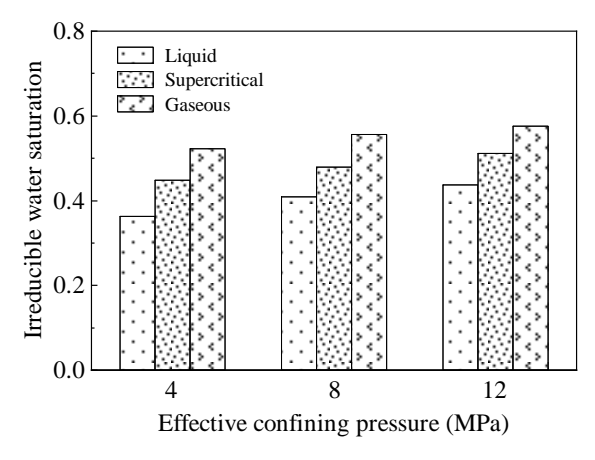


**Fig. 9**. Effect of effective confining pressure on irreducible water saturation.

8). The viscosity ratio can be determined using Eq. (5), and the capillary number (Ca) is expressed as:

$$Ca = \frac{\mu_i \nu}{\gamma} \tag{6}$$

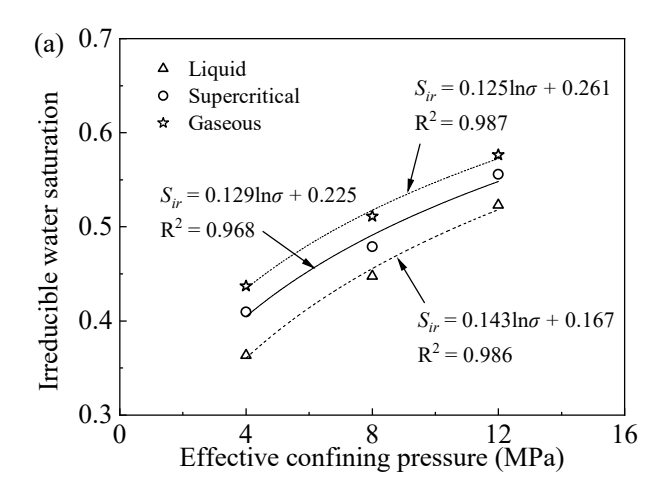
where v represents the Darcy velocity.

The classical  $\log \text{Ca} - \log M$  phase diagram divides the invasion patterns into four regimes: The upper-left region, where viscous forces dominate and viscous fingering occurs; the lower-right region, dominated by capillary forces leading to capillary fingering; the upper-right region of stable displacement; and the transitional zone of cross-fingering. Both Ca and M critically affect the invasion pattern, making either capillary or viscous fingering the predominant mechanism during displacement (Amiri and Hamouda, 2014). Since all experimental results fall within the capillary fingering area (Fig. 8), proving that the capillary force determines the invasion pattern, the residual water saturation observed in this study is primarily controlled by capillary forces. Therefore, Laplace's equation can be effectively applied to explain the dominant role of capillary effects in determining the existence of residual water rather than the viscosity ratio.

#### 3.3 Influence of effective confining pressure

The variations in formation depth and pore pressure changes induced by CO<sub>2</sub> injection lead to significant alterations in the effective confining pressure. Consequently, the reservoir pore structure is modified, exerting a significant impact on the irreducible water saturation. Fig. 9 illustrates the relationship between effective confining pressure and irreducible water saturation for gaseous, supercritical, and liquid CO<sub>2</sub>. As the effective confining pressure increases, the irreducible water saturation rises significantly, with all three CO<sub>2</sub> phases following closely aligned trends.

To further quantitatively interpret these observed trends, especially given the challenges associated with directly measuring key parameters such as interfacial tension and contact angle, this study employs the density of CO<sub>2</sub> in different phases as a practical proxy to establish an empirical correlation with residual water saturation. This approach allows us to elucidate the combined effects of effective confining pressure



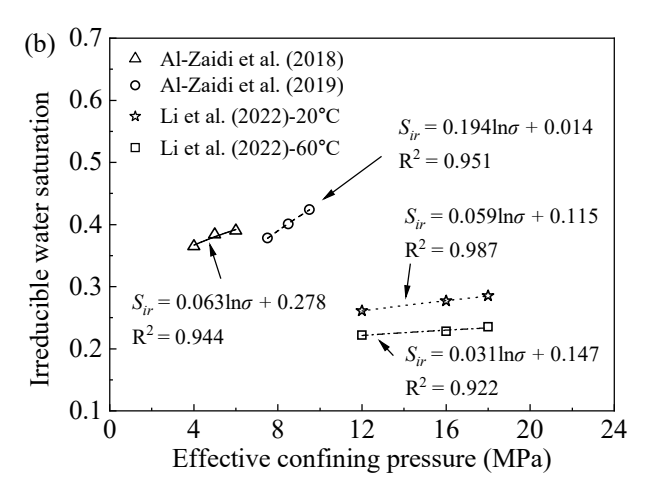


Fig. 10. Effects of variation in effective confining pressure on irreducible water saturation: Validation against (a) experimental data from this study and (b) literature data.

and  $CO_2$  phase state. Accordingly, an empirical model has been developed that integrates  $CO_2$  density (reflecting  $CO_2$  phase state) and pressure to predict residual water saturation, as follows:

$$S_{ir} = (a + b\rho) \ln \sigma + ce^{\rho} \tag{7}$$

where  $S_{ir}$  refers to the irreducible water saturation;  $\sigma$  denotes effective confining pressure;  $\rho$  denotes the  $CO_2$  density under different phase states; and a, b and c are the fitting coefficients. The CO<sub>2</sub> phase state and the effective confining pressure collectively affect the irreducible residual water saturation. The greater the effective confining pressure and the lower the CO<sub>2</sub> density are, the greater the irreducible residual saturation in the core. Correspondingly, the proposed empirical model shows good agreement with our experimental data, with R<sup>2</sup> values as high as 0.987, 0.968, 0.986, respectively, for the three phases (Fig. 10(a)). To further validate the performance of the model, its robustness was evaluated against additional experimental datasets (Al-Zaidi et al., 2018, 2019; Li et al., 2022). The model accurately reproduces the increasing trend of irreducible water saturation with effective confining pressure (Fig. 10(b)), with R<sup>2</sup> values under different conditions reaching 0.944, 0.951, 0.997, and 0.922, respectively. Overall, the strong agreement between predictions and measurements confirms the reliability and broad applicability of the model.

A further analysis of the microscopic mechanisms governing the effect of effective confining pressure on residual water formation is presented in Fig. 11. Increasing effective stress induces the slight deformation of the core, reducing porosity and progressively compresses the volume of pores and throats. Consequently, the average capillary radius within the core gradually decreases. Fig. 11(a) shows the diameters of selected pore throats ( $r_{01}$ ,  $r_{02}$ ,  $r_{03}$ ) under low effective confining pressure, while Fig. 11(b) displays the same throats ( $r_{11}$ ,  $r_{12}$ ,  $r_{13}$ ) under high effective confining pressure. A clear comparison reveals that high stress causes pore throat constriction, leading to a noticeable reduction in the diameters ( $r_{01} > r_{11}$ ,  $r_{02} > r_{12}$ ,  $r_{03} > r_{13}$ ). Under high effective

stress, some initially open pore throats become constricted or completely closed, forming isolated "dead pores." This process increases the overall capillary pressure and expands the network of water-trapping capillaries, thereby enhancing water retention within the rock. As a result, irreducible water saturation rises with increasing effective confining pressure.

The concept of "dead pores" is essential for understanding stress-dependent water trapping. As illustrated in Fig. 11, a dead pore forms when the mechanical compression of a connecting throat hydraulically isolates a pore body from the main flow paths (Fig. 11(b)). Once isolated, the water trapped inside becomes immobile and cannot be displaced by invading CO<sub>2</sub>, thereby directly contributing to the irreducible water saturation of the rock. This mechanism is particularly important in ductile or poorly cemented formations, where pore throats are prone to deformation under changing reservoir stress conditions.

#### 3.4 CO<sub>2</sub> storage efficiency and capacity

A fundamental question in geological carbon storage is how to accurately predict the storage capacity and distribution of injected CO<sub>2</sub> of a target reservoir. Therefore, gaining a fundamental understanding of irreducible water saturation is essential to address this challenge, as it directly governs the accurate prediction of CO<sub>2</sub> plume migration and the reliable evaluation of storage efficiency (Bachu, 2015). The storage efficiency, defined as the ratio of injected CO<sub>2</sub> volume to the reservoir pore volume, can thus be expressed at the pore scale in terms of water saturation as:

$$E = 1 - S_w \tag{8}$$

When the residual water saturation in the reservoir is small enough (irreducible residual water saturation,  $S_{ir}$ ) during  $CO_2$  injection and storage, the  $CO_2$  storage efficiency reaches its maximum:  $E \le 1 - S_{ir}$ .

The relationship between CO<sub>2</sub> phase state and storage efficiency across varying effective confining pressures (4, 8,

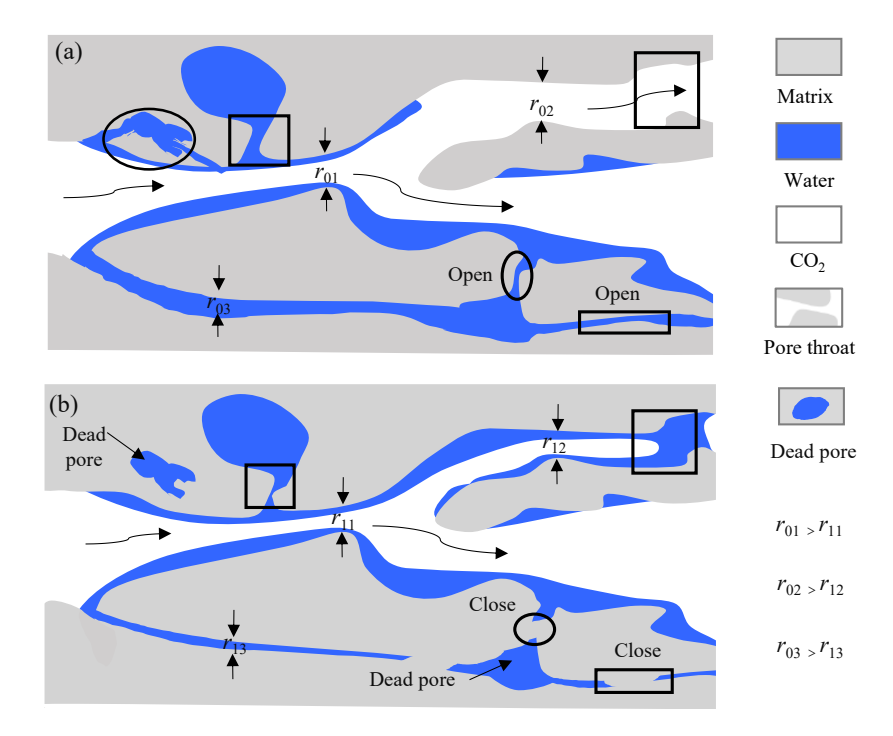
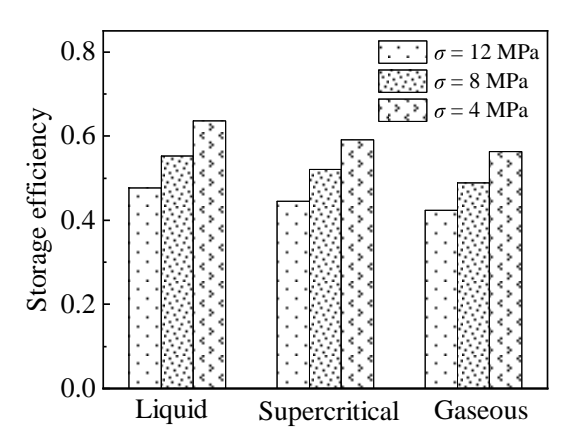


Fig. 11. Mechanisms of the influence of effective confining pressure on residual water saturation under (a) low and (b) high effective confining pressure.



**Fig. 12**. Effect of CO<sub>2</sub> phase state on CO<sub>2</sub> storage efficiency under different effective confining pressures.

and 12 MPa) is shown in Fig. 12, which illustrates that the efficiency follows the order of gaseous < supercritical < liquid. Furthermore, all three phases exhibit a similar decline in efficiency with increasing pressure. This trend is driven by the rise in capillary pressure under higher effective confining pressure, which enhances the ability of the rock to bind water and in turn reduces the pore space available for CO<sub>2</sub>, thereby diminishing storage efficiency.

Labus et al. (2015) conducted a simple calculation of storage capacity in the reservoir:

$$G = Ah\phi \rho E \tag{9}$$

where A represents area of a region assessed for CO<sub>2</sub> storage, h represents the thickness of aquifer formation, and  $\phi$  is average porosity.

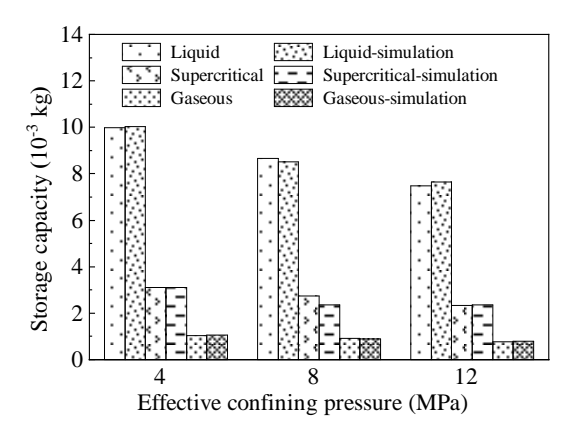


**Fig. 13**. Effect of CO<sub>2</sub> phase state on CO<sub>2</sub> storage capacity under different effective confining pressures.

Therefore, the formula for calculating the amount of  $CO_2$  in the core in this study can be expressed as:

$$G = V \phi \rho E \tag{10}$$

where V is the core volume.

With increasing effective confining pressure,  $CO_2$  storage capacity tends to decrease, and the  $CO_2$  phases have the same trend of  $CO_2$  storage capacity, that is, liquid > supercritical > gaseous (Fig. 13). Moreover, the values calculated from the formula correspond closely to the experimental measurements. The  $CO_2$  storage capacity of liquid  $CO_2$  in natural cores is approximately 3.2 times that of the supercritical phase and 9.6 times that of the gaseous phase, which strongly suggests that storing  $CO_2$  in the liquid phase can significantly enhance the overall storage capacity.

The scientific evaluation of storage capacity is essential for

geological CO<sub>2</sub> sequestration, requiring accurate evaluation under different thermodynamic states. When multiple CO<sub>2</sub> phases (including gaseous, critical-point, and liquid states) are injected, the injection in gaseous or supercritical states demands higher energy input (Vilarrasa et al., 2013). In comparison, the injection of liquid CO<sub>2</sub> reduces energy consumption due to its low compressibility, which minimizes compression work at the wellhead. Furthermore, liquid CO<sub>2</sub> has a higher density than supercritical CO<sub>2</sub>, which consequently reduces the *in-situ* fluid volume displaced. This leads to a smaller pressure drop at the wellhead and within the reservoir formation.

Therefore, it is concluded that liquid CO<sub>2</sub> injection is the preferred strategy under the appropriate reservoir conditions, as it maximizes storage efficiency and capacity while enhancing injectivity and mitigating risks. In summary, an indepth understanding of the drainage characteristics is of great significance to optimize storage strategy in different geological reservoirs and improve CO<sub>2</sub> storage efficiency. By accurately controlling and predicting residual water saturation, it is possible to manage the underground distribution more effectively, mitigate risks associated with enhanced oil recovery processes or CO<sub>2</sub> storage operations, and ultimately ensure long-term security.

#### 4. Conclusions

The efficiency and safety of  $CO_2$  geological storage are largely governed by residual water saturation, which varies with  $CO_2$  phase and subsurface stress conditions. The drainage experiments conducted in this study clarify how these factors interact, offering practical guidance for optimizing storage operations.

The results of this study demonstrate that residual water saturation is jointly controlled by CO<sub>2</sub> phase and effective confining pressure. Specifically, gaseous CO<sub>2</sub> yields the highest residual water saturation, followed by supercritical and liquid phases. Lowering the effective confining pressure also consistently reduces residual water saturation, regardless of the CO<sub>2</sub> phase.

Capillary forces are identified as the primary mechanism controlling residual water saturation. Higher interfacial tension or contact angle cosine values increase the capillary entry pressure, hindering CO<sub>2</sub> displacement and raising residual water saturation. Additionally, increased confining pressure compresses pore throats, forming "dead pores" that enhance capillary trapping.

An empirical model incorporating both the CO<sub>2</sub> phase and confining pressure reliably predicts residual water saturation. The findings indicate that liquid CO<sub>2</sub> injection under lower pressure offers the highest storage efficiency and capacity. Therefore, where reservoir conditions allow, liquid CO<sub>2</sub> injection is the preferred method to improve injectivity and storage security. These outcomes provide key criteria for selecting reservoirs for CO<sub>2</sub> storage and enhanced oil recovery.

#### Acknowledgements

The authors gratefully acknowledge the financial support provided by the National Key R&D Program of China (No. 2023YFB4203300) and the National Natural Science Foundation of China (No. 52238008).

#### **Conflict of interest**

The authors declare no competing interest.

**Open Access** This article is distributed under the terms and conditions of the Creative Commons Attribution (CC BY-NC-ND) license, which permits unrestricted use, distribution, and reproduction in any medium, provided the original work is properly cited.

#### References

- Al-Zaidi, E., Nash, J., Fan, X. Effect of CO<sub>2</sub> phase on its water displacements in a sandstone core sample. International Journal of Greenhouse Gas Control, 2018, 71: 227-238.
- Al-Zaidi, E., Nash, J., Fan, X. Gaseous CO<sub>2</sub> behaviour during water displacement in a sandstone core sample. International Journal of Greenhouse Gas Control, 2019, 80: 32-42.
- Aminu, M., Nabavi, S., Rochelle, C., et al. A review of developments in carbon dioxide storage. Applied Energy, 2017, 208: 1389-1419.
- Amiri, H., Hamouda, A. Pore-scale modeling of nonisothermal two phase flow in 2D porous media: Influences of viscosity, capillarity, wettability and heterogeneity. International Journal of Multiphase Flow, 2014, 61: 14-27.
- Bachu, S. Drainage and imbibition CO<sub>2</sub>/brine relative permeability curves at *in-situ* conditions for sandstone formations in western Canada. Energy Procedia, 2013, 37: 4428-4436.
- Bachu, S. Review of CO<sub>2</sub> storage efficiency in deep saline aquifers. International Journal of Greenhouse Gas Control, 2015, 40: 188-202.
- Bachu, S., Bennion, D. Dependence of CO<sub>2</sub>-brine interfacial tension on aquifer pressure, temperature and water salinity. Energy Procedia, 2009, 1: 3157-3164.
- Basirat, F., Yang, Z., Niemi, A. Pore-scale modeling of wettability effects on CO<sub>2</sub>-brine displacement during geological storage. Advances in Water Resources, 2017, 109: 181-195.
- Cai, J., Berg, S. Recent advances in flow through porous media for energy exploitation. Energy & Fuels, 2025, 39: 9181-9184.
- Cai, J., Qin, X., Wang, H., et al. Pore-scale investigation of forced imbibition in porous rocks through interface curvature and pore topology analysis. Journal of Rock Mechanics and Geotechnical Engineering, 2025, 17: 245-257.
- Herring, A., Andersson, L., Newell, D., et al. Pore-scale observations of supercritical CO<sub>2</sub> drainage in bentheimer sandstone by synchrotron X-ray imaging. International Journal of Greenhouse Gas Control, 2014, 25: 93-101.
- Jayasekara, D., Ranjith, P., Wanniarachchi, W., et al. Understanding the chemico-mineralogical changes of caprock sealing in deep saline CO<sub>2</sub> sequestration environments: A review study. The Journal of Supercritical Fluids, 2020, 161: 104819.

- Jung, J., Wan, J. Supercritical CO<sub>2</sub> and ionic strength effects on wettability of silica surfaces: Equilibrium contact angle measurements. Energy & Fuels, 2012, 26: 6053-6059.
- Kim, K., Kim, M., Oh, J. Core-scale investigation of the effect of heterogeneity on the dynamics of residual and dissolution trapping of carbon dioxide. Journal of Hydrology, 2021, 596: 126109.
- Kim, K., Oh, J., Han, W., et al. Two-phase flow visualization under reservoir conditions for highly heterogeneous conglomerate rock: A core-scale study for geologic carbon storage. Scientific Reports, 2018, 8(1): 4869.
- Kuo, C., Benson, S. M. Numerical and analytical study of effects of small scale heterogeneity on CO<sub>2</sub>/brine multiphase flow system in horizontal corefloods. Advances in Water Resources, 2015, 79: 1-17.
- Labus, K., Tarkowski, R., Wdowin, M. Modeling gas-rockwater interactions in carbon dioxide storage capacity assessment: A case study of Jurassic sandstones in Poland. International Journal of Environmental Science and Technology, 2015, 12: 2493-2502.
- Leung, D., Caramanna, G., Maroto-Valer, M. An overview of current status of carbon dioxide capture and storage technologies. Renewable and Sustainable Energy Reviews, 2014, 39: 426-443.
- Li, Y., Lv, L., Ming, L., et al. Quantitative investigation of phase characteristic effects on CO<sub>2</sub> breakthrough pressures in unsaturated Low-Permeability sandstone. Journal of Hydrology, 2022, 609: 127780.
- Li, Y., Ranjith, P.G., Perera, et al. Residual water formation during the CO<sub>2</sub> storage process in deep saline aquifers and factors influencing it: A review. Journal of CO<sub>2</sub> Utilization, 2017, 20: 253-262.
- Lu, Z., Zeng, C., Zhang, Y., et al. Study of the pore size influence on infiltration of porous media considering capillary effect. Capillarity, 2025a, 14(1): 1-12.
- Lu, Z., Wang, L., Guo, Z., et al. The microfluidic in geoenergy resources: Current advances and future perspectives. Advances in Geo-Energy Research, 2025b, 16(2): 171-180.
- Mazzotti, M., Pini, R., Storti, G. et al. Carbon dioxide (CO<sub>2</sub>) sequestration in unmineable coal seams and use for enhanced coalbed methane recovery (ECBM). Developments & Innovation in Carbon Dioxide Capture & Storage Technology, 2010, 2: 127-165.
- Mejia, L., Mejia, M., Xie, C., et al. Viscous fingering of irreducible water during favorable viscosity two-phase displacements. Advances in Water Resources, 2021, 153: 103943.
- Nomeli, M., Riaz, A. A data driven model for the impact of interfacial tension and density variations on CO<sub>2</sub> storage capacity in geologic formations. Advances in Water Resources, 2017, 107: 83-92.
- Pan, B., Li, Y., Xie, L., et al. Role of fluid density on quartz wettability. Journal of Petroleum Science and Engineering, 2019, 172: 511-516.
- Ragui, K., Chen, L. Identification of implicit dynamics of supercritical CO<sub>2</sub> invasion in sub-regions of bench micro-

- models. The Journal of Supercritical Fluids, 2023, 195: 105863.
- Samara, H., Liostrowski, T., Vganzer, L., et al. Unconventional oil recovery from Al Sultani tight rock formations using supercritical CO<sub>2</sub>. The Journal of Supercritical Fluids, 2019, 152: 104562.
- Saraji, S., Piri, M., Goual, L. The effects of SO2 contamination, brine salinity, pressure, and temperature on dynamic contact angles and interfacial tension of supercritical CO<sub>2</sub>/brine/quartz systems. International Journal of Greenhouse Gas Control, 2014, 28: 147-155.
- Shi, J., Xue, Z., Durucan, S. Supercritical CO<sub>2</sub> core flooding and imbibition in Berea sandstone-CT imaging and numerical simulation. Energy Procedia, 2011, 4: 5001-5008.
- Singh, K., Bijeljic, B., Blunt, M. Imaging of oil layers, curvature and contact angle in a mixed-wet and a water-wet carbonate rock. Water Resources Research, 2016, 52(3): 1716-1728.
- Spycher, N., Pruess, K., Ennis-King, J. CO<sub>2</sub>-H<sub>2</sub>O mixtures in the geological sequestration of CO<sub>2</sub>. I. Assessment and calculation of mutual solubilities from 12 to 100 °C and up to 600 bar. Geochimica et Cosmochimica Acta, 2003, 67: 3015-3031.
- Sun, X., Bi, Y., Guo, Y., et al. CO<sub>2</sub> geo-sequestration modeling study for contact angle estimation in ternary systems of brine, CO<sub>2</sub>, and mineral. Journal of Cleaner Production, 2021, 283: 124662.
- Vilarrasa, V., Silva, O., Carrera, J., et al. Liquid CO<sub>2</sub> injection for geological storage in deep saline aquifers. International Journal of Greenhouse Gas Control, 2013, 14(14): 84-96.
- Xu, L., Li, Q., Myers, M., et al. Flow behavior characteristics and residual trapping of supercritical carbon dioxide in tight glutenite by MRI experiments. Journal of Natural Gas Science and Engineering, 2020, 83: 103540.
- Yang, Y., Wang, J., Wang, Q., et al. Pore-scale numerical simulation of supercritical CO<sub>2</sub>-brine two-phase flow based on VOF method. Natural Gas Industry B, 2023, 10(5): 466-475.
- Yiotis, A., Psihogios, J., Kainourgiakis, M., et al. A lattice boltzmann study of viscous coupling effects in immiscible two-phase flow in porous media. Colloids & Surfaces A Physicochemical & Engineering Aspects, 2007, 300(1-2): 35-49.
- Zadeh, S., Egan, V., Walsh, P. Experimentally investigating the pressure drop of liquid-liquid Taylor flows over varying viscosity ratios. International Journal of Multiphase Flow, 2024, 170: 104629.
- Zeng, C., Zhang, Y., Lu, H., et al. Simulation of CO<sub>2</sub>-water two-phase fluid displacement characteristics based on Phase Field Method. Deep Underground Science and Engineering, 2025, 3(2): 1-14.
- Zhang, L., Chen, L., Hu, R., et al. Subsurface multiphase reactive flow in geologic CO<sub>2</sub> storage: Key impact factors and characterization approaches. Advances in Geo-Energy Research, 2022, 6(3): 179-180.